Improving molten regolith electrolysis with zirconia-based hollow anode technology

Kevin Yu[1], William West[2], Jamesa Stokes[3], Bryan Harder[3],

Lorlyn Reidy[4], Jesus Dominguez[4], Katherine T. Faber[1]

[1]Division of Engineering and Applied Science, California Institute of Technology, Pasadena, California, USA

[2]Jet Propulsion Laboratory, California Institute of Technology, Pasadena, California, USA

[3]NASA Glenn Research Center, Cleveland, Ohio, USA

[4]NASA Marshall Space Flight Center, Huntsville, Alabama, USA

*Corresponding author: Katherine Faber (ktfaber@caltech.edu)

Abstract

Molten regolith electrolysis is a promising in-situ resource utilization technology that targets O_2 and metals production through the direct electrolysis of molten lunar regolith. However, there are still challenges associated with molten regolith electrolysis, such as bubble detachment and O_2 separation and collection at the anode. A hollow anode, comprised of an oxygen-conducting yttria-stabilized zirconia shell and a platinum current collector, is designed here to address these challenges. Experimental results from an inverted hollow anode reactor successfully demonstrate that molten regolith electrolysis can be performed through a solid electrolyte. The elemental composition of both the cathodic products (primarily Fe and Si) and solidified lunar regolith simulant are reported as a function of electrolysis duration. These observations are supported by a thermochemical model built using FactSage to provide compositions of the cathodic products and solidified regolith simulant with increasing O_2 removal. Finally, the behavior of yttria-stabilized zirconia in the hollow anode application is characterized, and provides guidance for the design and operation of a yttria-stabilized zirconia hollow anode to enable integration into a full-scale molten regolith electrolysis reactor.

1. Introduction

NASA's Artemis program seeks to return humans to the lunar surface for the first time since the Apollo program, with a long-term goal of establishing a sustainable human presence on the lunar surface [1]. In support of these goals, there has been a renewed focus on developing lunar in-situ resource utilization (ISRU) technologies that can extract and process lunar resources into valuable commodities. O_2 production on the lunar surface is considered a critical ISRU technology to enable a long-term lunar presence by reducing the cost of resupply launches to the lunar surface, while also curtailing the reliance on terrestrially-produced O_2 [2]. The O_2 may be used as breathable O_2 for astronauts as well as the oxidizer for launch vehicles such as NASA's Space Launch System and SpaceX's Starship and accounts for approximately 70% of the initial mass of these launch vehicles [3,4]. Any lunar-produced O_2 that can be refueled either on the lunar surface or in lunar orbit can provide significant cost savings in the long run [5].

Several O_2 production processes have been investigated, either targeting a feedstock of lunar regolith or lunar ice [6,7]. The present study focuses on a specific ISRU technology known as molten regolith electrolysis (MRE) that seeks to directly electrolyze molten lunar regolith, producing Fe-Si alloys at the cathode and O_2 at the anode [6,7]. MRE is a promising technology because it can achieve a high oxygen extraction efficiency and produces two useful commodities in O_2 and metals [8]. Guerrero-Gonzalez et al. performed a system analysis of different ISRU technologies targeting O_2 and metals production and found that MRE was the most effective ISRU process in terms of mass payback ratio [9].

However, there are still challenges associated with MRE, arising from its harsh operational environment. To fully melt lunar regolith, temperatures of approximately 1600°C are necessary [6]. At this temperature, contact with the corrosive molten regolith can cause

significant degradation to refractory materials [10]. This is further complicated at the anode, where O_2 generation causes an oxidizing environment at the anode surface, in addition to contact with molten regolith at 1600°C. An ideal MRE system would utilize inert anodes that do not degrade during operation. Unfortunately, there has not been a material identified that can completely resist corrosion by molten silicates at MRE operational temperature, while also being electrically conductive to enable electrolysis [11]. An alternative is to use a quasi-inert anode, with a controlled degradation rate, that would require periodic replacement. Reviews indicate that current MRE reactors utilize an Ir or Ir-coated quasi-inert anode to operate under these conditions [12,13]. Wang et al. investigated Ir corrosion rates when used as the anode in MRE and measured a corrosion rate of ~8 mm/year, which is lost through dissolution to the molten regolith electrolyte [14]. Given the high cost and scarcity of Ir metal, it is unclear if Ir anodes are a cost-effective solution for long-term MRE reactors.

In addition to the materials challenges at the anode, there are other inefficiencies when performing MRE on the lunar surface. The O_2 produced at the anode surface is formed at a liquid/solid interface and produces bubbles. The molten regolith has a high viscosity and surface tension while operation on the lunar surface reduces the acceleration due to gravity, resulting in a lower buoyancy force [15]. The combination of these factors indicates that it is more difficult for bubbles to separate from the anode surface. This effectively decreases the surface area of the anode and can potentially cause electrolysis to stall [16]. Burke et al. investigated bubble separation in MRE reactors and found that bubbles generally become larger and bubble detachment time increases with the reduced lunar gravity [17]. Beyond bubble separation, there is also a reduction in O_2 capture efficiency associated with bubbling O_2 through molten regolith into a shared reactor headspace. This allows O_2 to reoxidize partially reduced Fe^{2+} species in the

molten regolith electrolyte or gaseous reduced metal species, such as Na, K, or Mg in the reactor headspace, lowering the overall O_2 generation efficiency [15].

This study introduces a new type of anode, known as the hollow anode, that can mitigate some of the aforementioned risks associated with MRE. The hollow anode is designed to allow for the facile collection of O_2 after it has been produced through MRE. Figure 1(a) provides a schematic of the envisioned integration of a hollow anode in a MRE reactor, based on the work of Grossman et al. [18]. The hollow anode contains a solid electrolyte shell and a metallic current collector. Within this design, the goal is to force O^{2-} from the molten regolith to migrate through an oxygen-conducting solid electrolyte to the metallic current collector. Once O^{2-} reaches the current collector, electron transfer can occur, allowing for oxidation of O^{2-} into O_2. The generated O_2 is fully contained within the solid electrolyte shell, enabling the collection of O_2 without contact between the molten regolith and O_2. Additionally, O_2 is now generated at a solid/solid interface, eliminating the bubble formation challenges discussed earlier. The hollow anode design also prevents any volatile species from contaminating the electrolyzed, high-purity O_2.

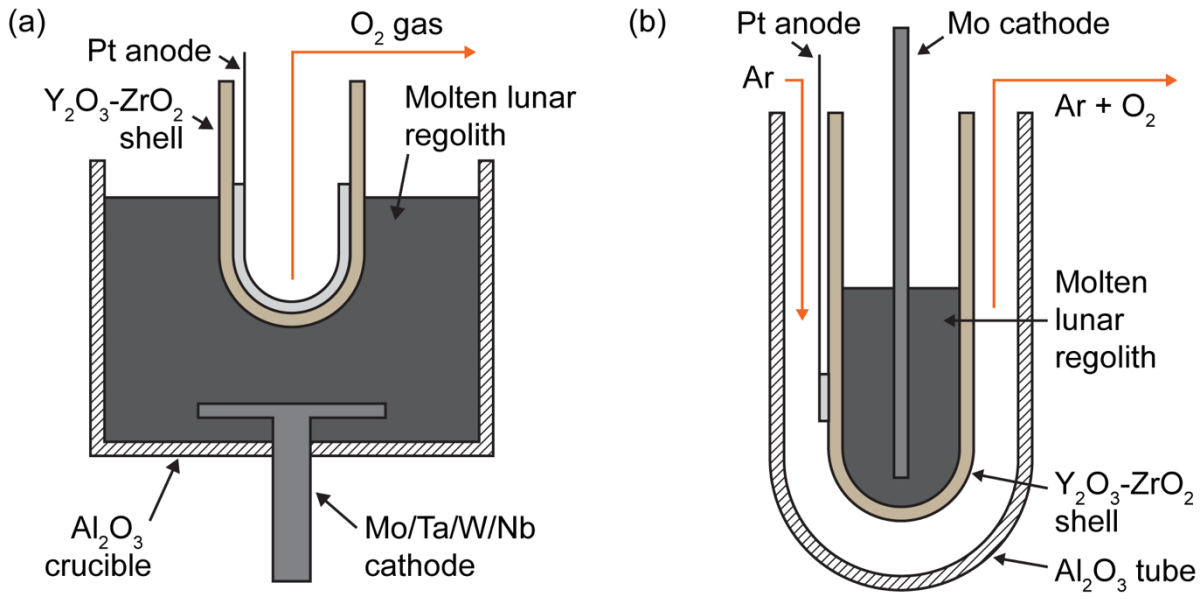

Figure 1: *Schematic of (a) envisioned integration of hollow anode into existing MRE reactors and (b) inverted hollow anode used to perform proof-of-principle experiments.*

The materials used for the hollow anode are yttria-stabilized zirconia (YSZ) for the solid electrolyte shell and Pt for the metallic current collector. YSZ is a well-known oxygen-ion conductor, as well as a refractory oxide ceramic. Previous work by the authors has shown that YSZ demonstrates controlled degradation in contact with molten regolith simulants at 1600°C [19]. Pt is used as the current collector since it is relatively resistant to oxidizing environments at high temperatures [20]. Unlike the Ir anodes discussed earlier, the Pt used in the hollow anode does not directly contact molten regolith, avoiding the dissolution of Pt into the molten regolith electrolyte. The combined YSZ/Pt anode shown in Figure 1(a) is referred to as the hollow anode.

Anodes with a similar design to the hollow anode have been used previously in lower temperature applications. Guo et al. studied the use of YSZ/Ag anodes in oxy-fluoride fluxes at 1200°C and found that the optical basicity of the oxy-fluoride flux has a significant effect on YSZ degradation [21]. Gao et al. investigated the use of magnesia-stabilized zirconia (MSZ)/Pt

anodes in FeO-containing slags at 1450°C and found that the inclusion of MSZ as a solid electrolyte does not negatively impact the performance of their electrolysis cell [22,23]. Both experiments were performed at lower temperatures than the MRE operational temperature of 1600°C. Moreover, the flux (Ca^{2+}, Mg^{2+}, Si^{4+}, Y^{3+}) or slag (Ca^{2+}, Mg^{2+}, Si^{4+}, Al^{3+}, Fe^{2+}/Fe^{3+}) used contained relatively few cationic species compared to the 10-component molten regolith simulant used in these experiments.

This work focuses on the design, fabrication and testing of a laboratory-scale MRE cell, utilizing an inverted hollow anode, which successfully demonstrates that MRE can be performed with a hollow anode for up to 12 hours. Residual gas analysis confirms the production of O_2 when potential is applied to the cell. The elemental composition of both the cathodic products and solidified regolith simulant are presented, indicating that FeO and SiO_2 are the primary oxide species being electrolyzed. A FactSage thermochemical model was also built to predict the cathodic products and remaining regolith simulant compositions, which is compared to the experimentally measured compositions from the MRE cells. The results of laboratory-scale testing reveal interactions between YSZ and molten regolith simulant that will be discussed and extended to provide design considerations for a hollow anode in full-scale MRE reactors.

2. Materials and methodology

2.1 Lunar regolith simulant

The lunar south pole is the targeted landing site for NASA's Artemis missions and could potentially be suitable for a permanent lunar settlement [24]. As a result, MRE experiments were performed on lunar highlands regolith simulant, which is more representative of the regolith at the lunar south pole [25]. LHS-1 (Space Resource Technologies) was selected as the highlands

regolith simulant. The composition of LHS-1 [26], and a comparison to lunar highlands regolith returned from Apollo 16 [27], are presented in Table 1. Though there are some compositional variations in specific oxides (CaO, MgO, Na_2O), the terrestrially-produced LHS-1 is comparable in the major oxides, SiO_2 and Al_2O_3, to the lunar regolith returned by Apollo 16. It is noted that though Table 1 presents the composition using a binary oxide basis, both the lunar regolith and regolith simulant are comprised of mixtures of oxide glasses and minerals. However, MRE seeks to fully melt the regolith to form an ionic liquid electrolyte and does not require the presence of specific minerals, such as ilmenite ($FeTiO_3$) for hydrogen reduction [28].

Table 1: *Major abundances of LHS-1 simulant and highlands lunar regolith (wt%)* [26,27]

Species	SiO_2	FeO	MgO	CaO	Al_2O_3	TiO_2	Na_2O	K_2O	MnO	P_2O_5
LHS-1 (Simulant)	51.2	2.7	1.6	12.8	26.6	0.6	2.9	0.5	0.1	0.1
Apollo 16 (#64501)	45.3	4.2	4.9	17.2	27.7	0.4	0.4	0.1	< 0.1	-

2.2 Molten regolith electrolysis experiments

All MRE runs were performed in the inverted hollow anode configuration, shown in Figure 1(b). In this design, the YSZ tube functioned as both the primary containment vessel and as the solid electrolyte for O^{2-}. An outer alumina tube was used to isolate the gaseous environment around the cell and acted as a secondary containment vessel. A mass flow controller (FMA series, OMEGA) was used to provide a consistent Ar flow to serve as the carrier gas. The gas outlet was connected to a residual gas analyzer (HPR-20, Hiden Analytical) for compositional analysis to track the production of O_2. The sealed electrolysis reactor was placed into a high-temperature box furnace (Rapid Temp Furnace, CM Furnaces) for heating to the

operational temperature. The electrolysis cell was designed such that the lower ¼ portion of the cell containing LHS-1 is exposed to operational temperature, as shown in Figure 1(b). The upper portion of the electrolysis reactor with electrical leads, gas fittings, and tube gaskets (not shown) remained near ambient temperature. A potentiostat (VersaStat 4, Princeton Applied Research) was attached to the cathode and anode leads to perform electrolysis. Labeled images showing the assembled cell in operation are provided in Supplementary Materials S1.

2.2.1 Electrolysis cell fabrication

A custom stainless steel endplate was designed and machined to provide a mounting point for the interior 10.5 wt% YSZ tube and a sealing surface for the exterior alumina tube (McDanel Advanced Material Technologies). The endplate also contained feedthroughs for the cathode, anode, gas inlet tube, and gas outlet tube. To fabricate the electrolysis cell, a YSZ tube was loaded with approximately 20 grams of LHS-1 and mounted onto the endplate. The cathode was an alumina-sheathed Mo rod that was inserted into the center of the endplate and pushed down the YSZ tube through the loose regolith simulant. The anode consisted of a Pt wire mesh that was adhered to the exterior of the YSZ tube with Pt ink (Fuel Cell Store). The gas inlet and outlet tubes were then attached to the endplate. Finally, the entire assembly was lowered into the exterior alumina tube and sealed off by a Viton gasket at the endplate.

2.2.2 Electrolysis conditions

MRE was performed for three different durations – 1 hour, 3 hours, and 12 hours. The operational temperature of the electrolysis cell was 1600°C for all three durations. The cell was held at temperature for an additional hour before and after electrolysis to allow the cell to stabilize before starting electrolysis and to perform electrochemical characterization such as cell resistance determination. The thermal profile of all three electrolysis durations is provided in

Supplementary Materials S2. All experiments were run under 100 sccm of flowing Ar. The experiments were performed with a constant current set at 0.5 A on the potentiostat. The cathode surface area is ~10 cm^2 and the anode pad surface area is ~1 cm^2, giving an anodic current density of ~0.5 A/cm^2. The YSZ tube, LHS-1 regolith simulant, Mo cathode, and Pt anode were replaced between each electrolysis test.

2.3 Characterization

The geometry of the MRE cells was designed to allow for characterization of all heated cell components, including the YSZ solid electrolyte, cathodic products, and solidified regolith simulant, after each experiment. After cooling, each cell was mounted in epoxy and cross-sectioned down the middle of the cell. One half of each cell was polished to 0.05 μm to prepare for subsequent characterization.

2.3.1 Optical microscopy

All cells were optically imaged at 30x (VHX-7000, Keyence) and stitched together to capture macroscopic changes resulting from high-temperature operation and electrolysis. Further investigation of regions of interest were performed at 50x – 200x (VHX-2000, Keyence). These regions of interest provided guidance for higher-magnification electron microscopy. ImageJ was used to measure YSZ wall recession from these images [29].

2.3.2 Electron microscopy

Scanning electron microscopy (SEM; 1550VP FESEM, ZEISS) was used with the backscattered electron (BSE) detector to image the cathodic products and solidified regolith simulant within each cell. BSE image brightness is determined by the average atomic number of the elements present, with lighter elements appearing darker. Since O has a low atomic number, BSE images can provide an initial analysis of which regions are metallic (the cathode and

cathodic products) vs. oxide (the remaining LHS-1). Energy dispersive X-ray spectroscopy (EDS; X-Max EDS, Oxford Instruments) was used to assess the elemental composition of the cathodic products and solidified regolith simulant using EDS mapping and point analysis.

Beyond SEM and EDS, electron backscatter diffraction (EBSD; HKL EBSD, Oxford Instruments) was used to determine the grain structure and phase of YSZ. Specifically, regions of YSZ in contact with molten regolith were analyzed to elucidate the compositional and microstructural changes of YSZ for each electrolysis cell. Each EBSD analysis region was 300 μm wide (along a YSZ/LHS-1 interface) and 700 μm deep (from YSZ/LHS-1 interface into YSZ interior) with a 1.5 μm step size. All electrolysis cells and a polished fragment of the beginning-of-life (BOL) YSZ were analyzed using EBSD. MTEX, an EBSD analysis software package, was used for grain segmentation and grain size analysis on the collected EBSD maps to provide statistical data on grain sizes [30].

2.3.3 Raman spectroscopy

A confocal Raman microscope (inVia Raman, Renishaw) was used on the center of the YSZ walls to qualitatively determine the effect of extended electrolysis on YSZ. All electrolysis cells and a fragment of the BOL YSZ were characterized by Raman spectroscopy. For this analysis, a 20x lens was used with 10% laser power, a 30-second acquisition time, with three total accumulations. Background subtraction was performed using the WiRE software package (Renishaw). The resulting data were normalized for intensity by MATLAB.

2.3.4 FactSage analysis

FactSage 8.3 was used to construct a thermochemical model for the removal of O_2 from molten lunar regolith at 1600°C [31]. The LHS-1 composition from Table 1 was input as the initial composition for the system, totaling 1 gram. The FToxid and FTlite databases were used to

determine the equilibrium slag (regolith simulant) and metal (cathodic products) compositions, respectively. Data for all solid and liquid solutions/compounds containing the species in Table 1 were added from both the Ftoxid and FTlite databases; however, only the slag and liquid metal phases were predicted to be thermodynamically stable at 1600°C. The gas phase was omitted to reduce computation time. The basis for O_2 removal is extraction efficiency and is defined as the mass of O_2 produced divided by the mass of regolith. The model was used to generate the equilibrium slag and metal compositions from an extraction efficiency of 0% (representing BOL) to 5%, in 0.1% increments. This was accomplished by setting O_2 as a variable species and allowing it to vary from 0 to -0.05 grams, representing 0% and 5% extraction efficiency. It is noted that these results do not account for the kinetics of electrolysis and are only able to determine the thermodynamic equilibrium composition assuming that O_2 is removed from the system. As a result, Mo (cathode) and YSZ/Pt (anode) are not included in this analysis since their dissolution into the molten LHS-1 is a kinetically limited process.

3. Results

3.1 Electrolysis data

The volumetric percentage of O_2 in the outlet gas stream and the potential required to maintain 0.5 A of current through the cell are presented in Figure 2. Elapsed time in these plots is counted from the application of constant current to the cell. In all cells, the O_2 content increased from ~0.005 vol% (background O_2) to ~1 vol% within a few minutes of starting electrolysis. The constant current condition was applied for 1 hour, 3 hours, and 12 hours. The time at which the potential curve terminates denotes the end of electrolysis. Within a few minutes of ending electrolysis, the O_2 content decreases to ~0.005 vol%. These results indicate that O_2 is being produced when current is applied to the cell, providing a proof-of-principle validation that MRE

can be performed through the YSZ solid electrolyte and demonstrating that the hollow anode design is feasible.

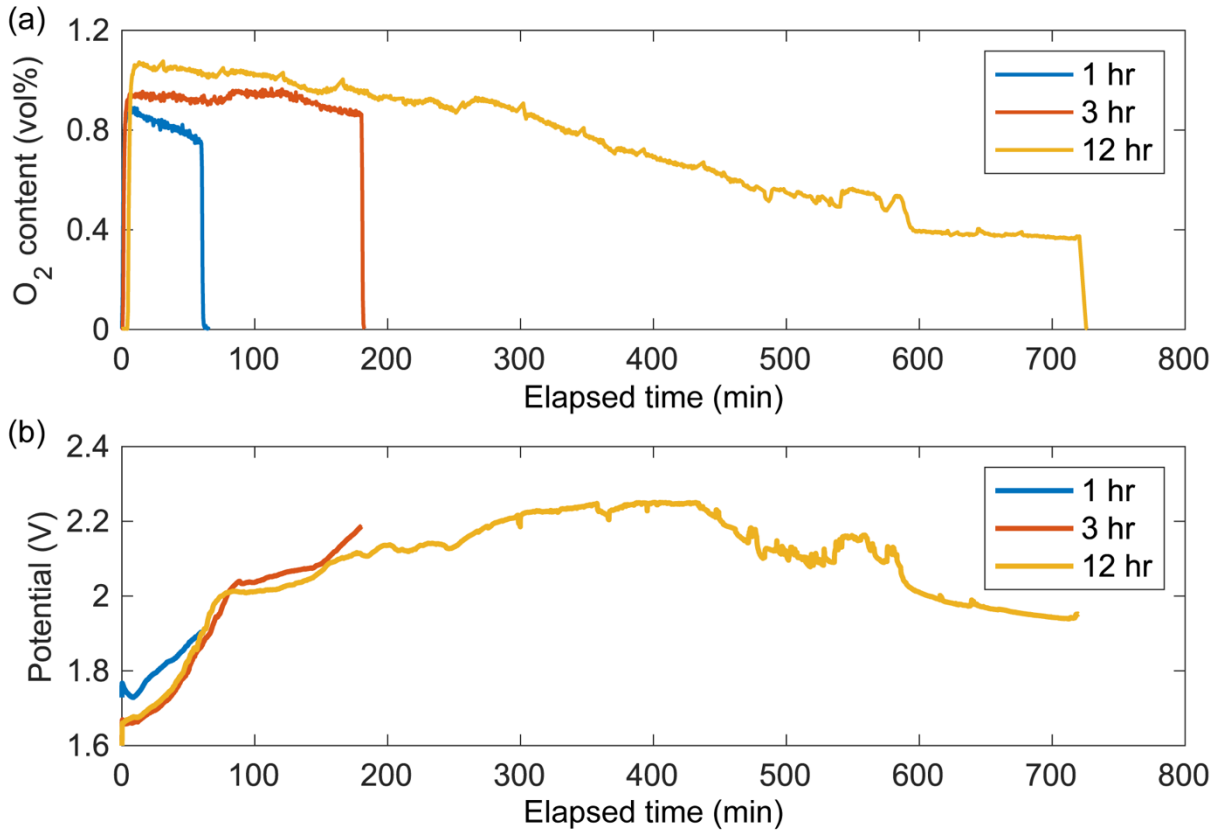

Figure 2: *(a) O_2 content of outlet gas stream and (b) potential across electrolysis cell vs. elapsed time since electrolysis start for all three electrolysis experiments.*

The initial potential behavior for the three electrolysis cells is comparable, suggesting that the electrolysis cell fabrication procedure is robust. All three cells exhibited an increase in potential over the first ~80 minutes of operation. In this initial period, the expected cathodic reaction is the reduction of Fe^{2+}/Fe^{3+}, coming from FeO/Fe_2O_3 in the regolith. The increase in potential is attributed to two factors – the mass transport limitation of FeO/Fe_2O_3 and the increase in regolith viscosity. When electrolysis first occurs, the molten regolith is well-mixed, with FeO/Fe_2O_3 available at the cathode surface for reduction. As electrolysis continues, the FeO/Fe_2O_3 concentration near the cathode surface is depleted as it is reduced to Fe^0, requiring a

larger potential to cause FeO/Fe_2O_3 to migrate to the cathode. In addition to this effect, FeO/Fe_2O_3 is also a glass network modifier which increases regolith viscosity with decreasing concentration [32]. Thus, as FeO/Fe_2O_3 is depleted from the molten regolith, the viscosity of the remaining molten regolith increases, which requires the potential to further increase in order to maintain a consistent rate of FeO/Fe_2O_3 diffusion to the cathode surface.

In the 3-hour and 12-hour electrolysis cells, there is an inflection point in the potential curve at approximately 90 minutes. Based on FactSage predictions (Section 3.4), this inflection point is an indication that nearly all the FeO/Fe_2O_3 in LHS-1 has been electrolyzed. After this point, Si^{4+} reduction, from SiO_2, becomes the dominant cathodic reaction, which is consistent with previously reported models [15]. Due to the significantly higher concentration of SiO_2 compared to FeO in LHS-1, the limitation on mass transport is diminished, causing the potential to increase at a slower rate after the inflection point. In contrast to FeO/Fe_2O_3, SiO_2 is a glass network former. The continued removal of SiO_2 through electrolysis causes the regolith viscosity to decrease, thereby increasing the diffusivity of cations in the remaining regolith, allowing more SiO_2 to diffuse to the cathode surface. These two effects result in a slower increase in the potential applied after the inflection point in both the 3-hour and 12-hour electrolysis cells.

The 12-hour electrolysis cell potential alone indicates that its slower rate of increase continues until ~420 minutes (7 hours) of electrolysis. At this point, the potential starts to decrease and contains more noise. The decrease in potential is associated with a lower cell resistance, which is attributed to the onset of electronic conductivity in YSZ and will be discussed in more detail in Section 3.5.2. The noise in the data is attributed to the expanding cathodic products. As more cathodic products are generated, its volume increases until an electronic short between the cathode and the YSZ wall is formed. Since the cathodic products are

liquid at operational temperature, the noise in the potential originates from shorts forming and disappearing as the liquid cathodic products are repositioned by natural convection within the cell.

In all three electrolysis experiments, the highest O_2 content measured occurs at the start of electrolysis and decreases over time. This behavior is also attributed to the onset of electronic conductivity in YSZ and is discussed in more detail in Section 3.5.2 [33–35]. As YSZ becomes more electronically conductive, O_2 is not solely generated on the exterior of the YSZ but can also be generated on the interior of the inverted hollow anode. The gas outlet tube samples from the exterior of the YSZ. Any O_2 that is produced on the interior of the cell will likely oxidize the exposed portion of the alumina-sheathed Mo cathode. Evidence of this behavior has been observed in the interior of the YSZ (Supplementary Materials S3). The oxidation of Mo produces volatile MoO_x, which then condenses in cold regions of the cell. Therefore, it is assumed that the O_2 measured by the residual gas analyzer is the lower bound of O_2 produced since it cannot detect the Mo oxidation products that have condensed on cold spots in the electrolysis cell.

The volume of O_2 produced can be calculated by integrating the O_2 content data with a known gas flow rate from the mass flow controller. The electrolysis duration can be used in conjunction with the known current applied to the cell to calculate the total charge transferred during electrolysis. The anodic half-reaction is assumed to be:

$$2\ O^{2-} \rightarrow O_{2(g)} + 4\ e^-$$

The total charge transferred can be used to determine the maximum O_2 that could be produced by assuming that every e^- participates in the Faradaic reaction. The anodic Faradaic efficiency then can be calculated by dividing the measured O_2 produced by the theoretical maximum O_2 produced. Extraction efficiency is defined as the mass of O_2 produced divided by the mass of

regolith processed, with the maximum possible extraction efficiency for LHS-1 being approximately 46%. A summary of the aforementioned calculations and experimental measurements for each electrolysis experiment is presented in Table 2.

Table 2: *Summary of cathodic products and regolith electrolysis efficiencies*

Electrolysis duration	Cathodic products observed	Anodic Faradaic efficiency	Mass of O_2 produced	Extraction efficiency
1 hr	Fe	47%	0.070 g	0.4%
3 hr	Fe, P, Si	53%	0.237 g	1.2%
12 hr	Fe, P, Si, Ti, Mn	42%	0.749 g	3.7%

Hollow anodes incorporating an ideal O^{2-} ion conductor as the solid electrolyte would result in a Faradaic efficiency of 100% since the solid electrolyte blocks e^- transport. However, the onset of electronic conductivity in the YSZ used in these experiments causes the Faradaic efficiency to be lower than 100% since e^- are no longer blocked. Despite this behavior, the calculated anodic Faradaic efficiencies are in line with those reported in studies utilizing a bare Ir anode instead of a hollow anode. Sirk et al. performed MRE with a Mo cathode and Ir anode, reporting Faradaic efficiencies of approximately 30-60% when electrolyzing an FeO-containing molten regolith [36]. This suggests that the increased electronic conductivity of YSZ does not significantly reduce the Faradaic efficiency of MRE when compared to an Ir anode. However, it is noted that the inclusion of YSZ as a solid electrolyte may require a higher overpotential compared to an exposed Ir anode.

3.2 Cathodic products

Optical microscope images of each electrolysis cell and EDS elemental maps of the cathodic products generated in each electrolysis cell are presented in Figures 3 (1-hour

electrolysis), 4 (3-hour electrolysis), and 5 (12-hour electrolysis). A quantitative EDS point analysis of each region is provided in Supplementary Materials (Figures S4-S6). The observed cathodic products are also summarized in Table 2. The EDS maps presented consist of the observed cathodic products, except for O and Al. Al_2O_3 is not able to be electrolyzed at these durations, so the O and Al maps are provided as an indication of the position of the remaining regolith in each EDS region.

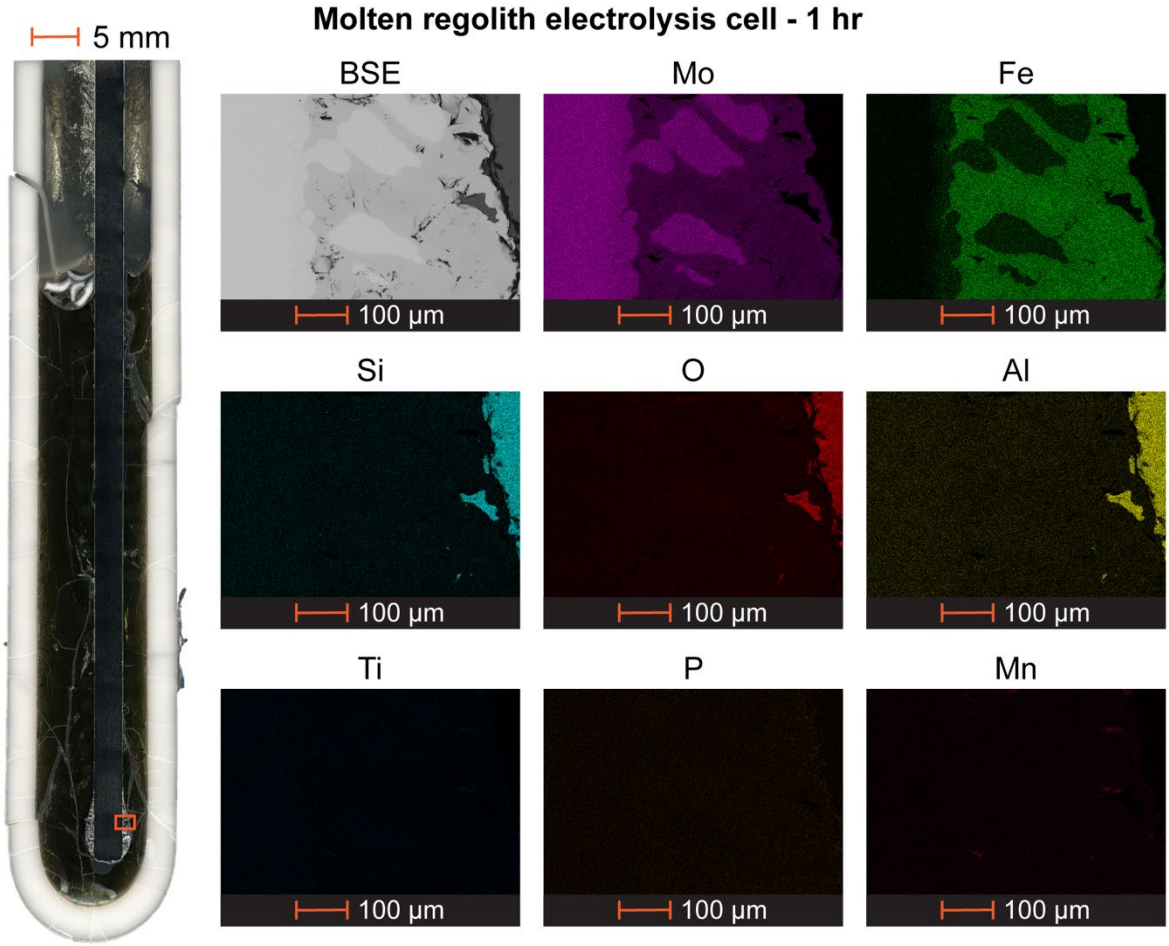

Figure 3: *Optical microscopy of the 1-hour electrolysis cell and EDS elemental maps of the cathodic products generated. EDS analysis area is denoted with the orange box in the optical microscope image.*

The EDS analysis for the 1-hour electrolysis cell indicates that Fe is the primary cathodic product. Figure 3 shows that there is a significant amount of Fe detected in the cathodic products, and it has alloyed with Mo from the cathode. The O EDS map in Figure 3 suggests that the Fe detected is Fe^0, not FeO/Fe_2O_3, since no O was detected in the cathodic products. The Fe and Mo maps also indicate that there are two different Fe-Mo alloys within the cathodic products. However, the bulb shape of the cathodic products (Figure 3) indicates that it is liquid at operational temperature, and likely phase separates on cooling, which is consistent with the Fe-Mo phase diagram [37]. No Si is detected within the cathodic products, which demonstrates that SiO_2 electrolysis has not been achieved in the 1-hour electrolysis cell.

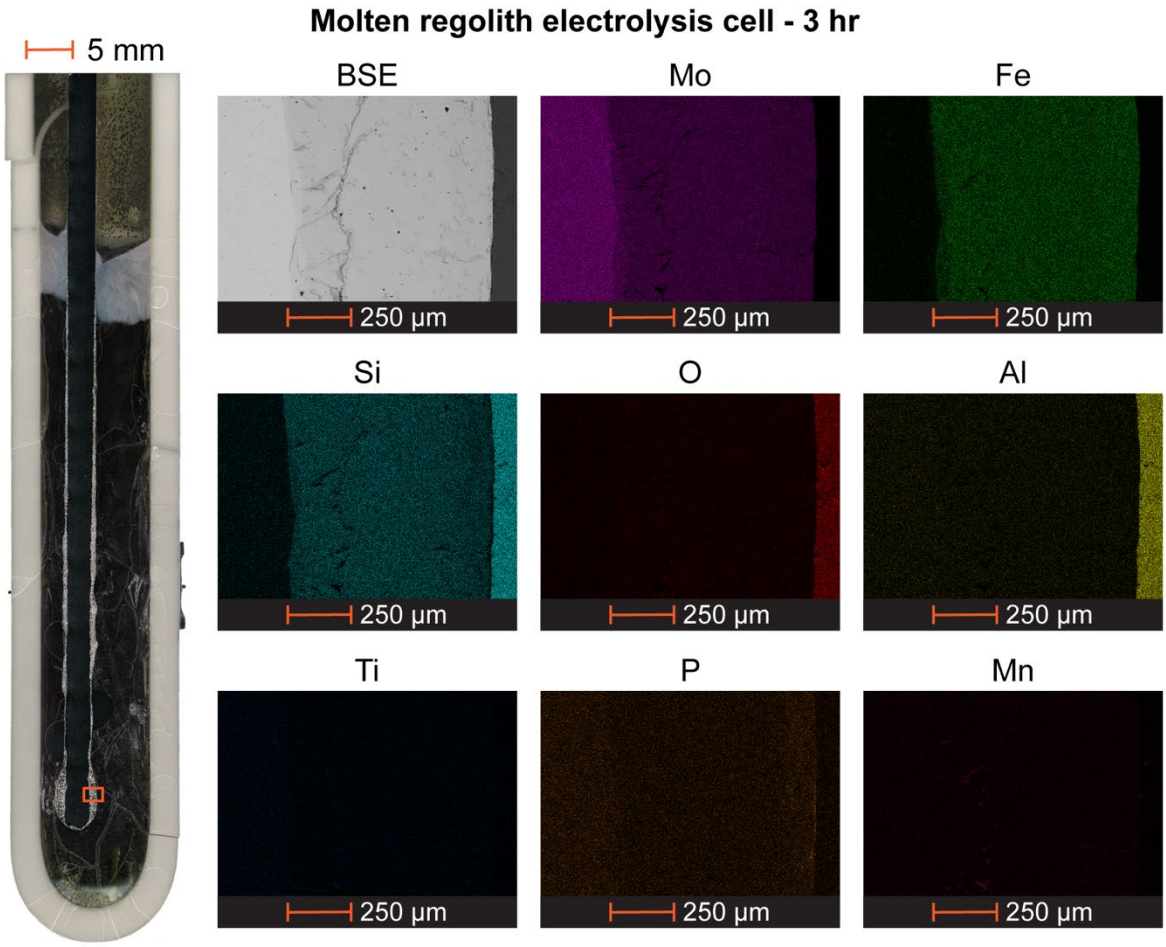

Figure 4: *Optical microscopy of the 3-hour electrolysis cell and EDS elemental maps of the cathodic products generated. EDS analysis area is denoted with the orange box in the optical microscope image.*

In contrast to the 1-hour electrolysis cell, EDS maps of the 3-hour electrolysis cell (Figure 4) show the presence of both Fe and Si in the cathodic products. Additionally, there is a detectable amount of P observed in the cathodic products. The Fe, Si, and P are also alloyed with Mo from the cathode. However, unlike the 1-hour cell (Figure 3), there does not appear to be significant phase separation in the cathodic products, indicating that the overall composition of the cathodic products is stable down to ambient temperature. The observation of Si in the cathodic products is significant since it indicates that SiO_2 electrolysis is being performed. To the

authors' awareness, this is the first reported experimental confirmation of Si production from the direct electrolysis of a molten lunar regolith simulant. Given that SiO_2 is the most abundant oxide species in LHS-1, this result provides a path for MRE with a hollow anode to achieve O_2 extraction efficiencies up to 25%.

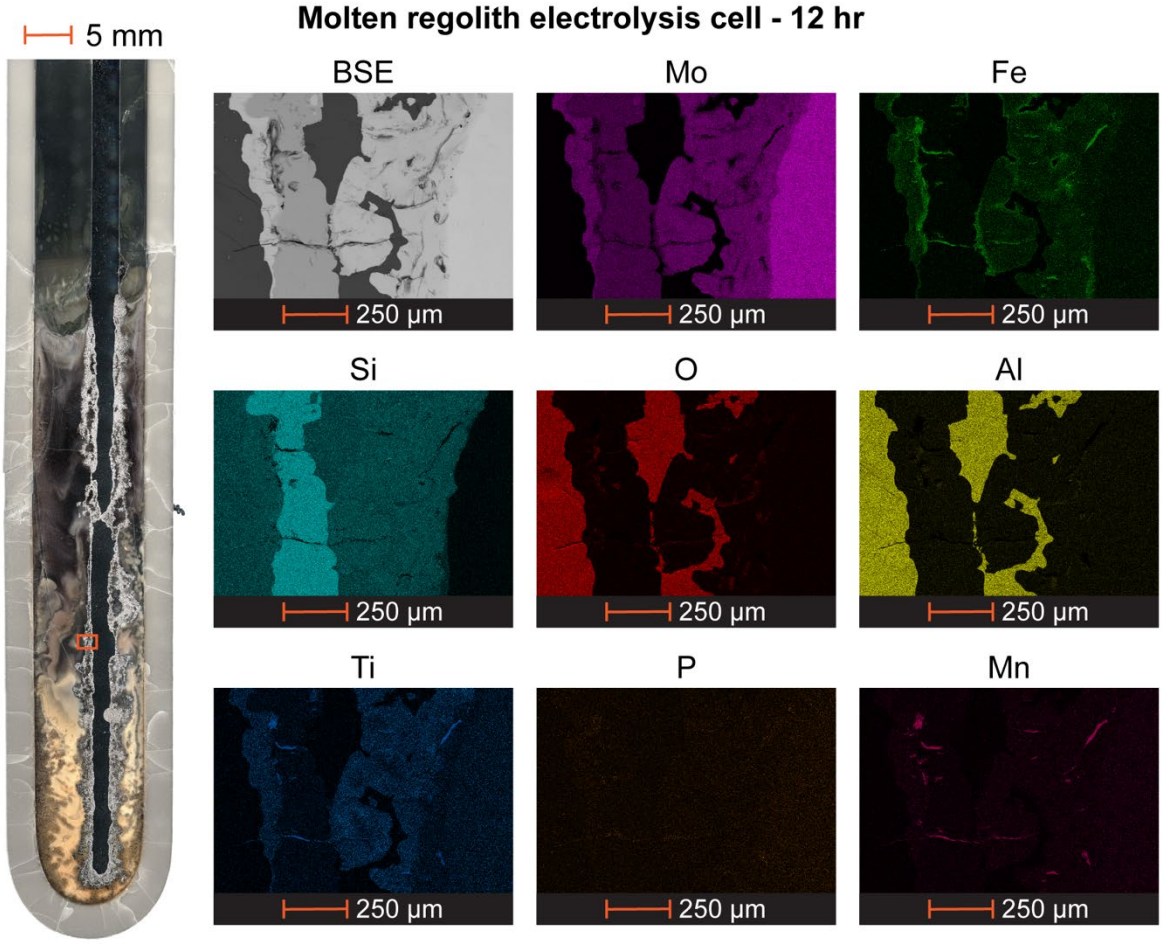

Figure 5: *Optical microscopy of the 12-hour electrolysis cell and EDS elemental maps of the cathodic products generated. EDS analysis area is denoted with the orange box in the optical microscope image.*

The cathodic products within the 12-hour electrolysis cell no longer form a dense film along the cathode surface and have begun migrating away from the cathode. Due to the cell design, there is likely a thermal gradient within the molten regolith. The top of the molten

regolith is expected to be cooler since it can radiate to the cold side of the electrolysis cell. The separation of the cathodic products from the cathode is attributed to the growing size of the liquid cathodic products layer. This results in a layer thickness that exceeds the flow boundary layer induced by convection from a thermal gradient, causing the cathodic products to be mixed with the remaining molten regolith.

Within the cathodic products, Ti and Mn are observed in addition to the previously observed Fe, Si, and P from the shorter duration electrolysis experiments. There is also now significant Si produced, such that Si in the cathodic products has a higher concentration (brighter in Si EDS map) than Si remaining in the molten regolith. A lower concentration of P is detected in the 12-hour electrolysis cell compared to the 3-hour electrolysis cell. Based on FactSage calculations (see Section 3.4), it is expected that P_2O_5 electrolysis occurs simultaneously with FeO reduction. Thus, by the end of the 3-hour electrolysis experiment, most of the P_2O_5 is likely already electrolyzed. The lower concentration of P in the 12-hour cell is attributed to dilution of the cathodic products with the continued production of Si.

The production of fully reduced cationic components from the molten regolith is expected for MRE. The presence of these reduced species in all three electrolysis cells provides further validation beyond O_2 production that MRE can be performed through a YSZ solid electrolyte. Though the production of these cathodic products is not the focus of the present study, it is important to confirm that the presence of YSZ at the anode does not significantly alter the expected cathodic half-reactions that balance the anodic half-reaction of O_2 production.

3.3 Solidified regolith analysis

Extended electrolysis of molten regolith alters the regolith composition since specific oxides in the regolith are preferentially reduced. The changing regolith (electrolyte) composition

can cause both the thermophysical properties (i.e. viscosity, density, etc.) and the electrical conductivity to vary from the beginning-of-life (BOL) LHS-1 properties. The average solidified LHS-1 composition for each of the three electrolysis cells was measured using EDS. These were compared to previous studies by the authors of the BOL composition of the molten LHS-1 when exposed to 1600°C in a YSZ crucible [19]. A comparison between the BOL composition and the post-electrolysis composition for each electrolysis experiment is presented in Table 3.

Table 3: *Average regolith composition after melting and electrolysis (at%)*

Species	Si	Fe	Mg	Ca	Al	Ti	Na	K	Y	Zr	O
BOL [19]	18.17	1.01	1.32	5.36	11.68	0.23	1.87	0.31	0.24	0.60	59.20
1 hr	18.21	0.47	1.30	5.23	11.70	0.22	1.90	0.32	0.17	0.47	60.01
3 hr	18.06	0.04	1.45	5.87	12.41	0.22	1.87	0.31	0.24	0.63	58.91
12 hr	15.23	0.00	1.78	7.21	12.95	0.17	2.32	0.34	0.37	0.66	58.97

The composition changes detected in LHS-1 are consistent with the observed cathodic products. A clear decrease in Fe concentration is detected from BOL to 12 hours of electrolysis, which is expected since Fe is electrolyzed across all three electrolysis experiments. A minor reduction in the Si concentration is detected in the 3-hour electrolysis cell and becomes a significant reduction in the 12-hour electrolysis cell, consistent with the continued electrolysis of SiO_2. The Ti concentration is consistent with BOL across the 1-hour and 3-hour electrolysis results but begins to decrease in the 12-hour electrolysis result, also consistent with the observation of Ti in the cathodic products of the 12-hour electrolysis result. Across all electrolysis experiments and the BOL specimen, Y and Zr are detected due to the dissolution of YSZ by molten regolith. This is discussed in further detail in Section 3.5.1.

3.4 FactSage thermochemical results

The FactSage thermochemical predictions of O_2 removal from LHS-1 are presented in Figure 6. The full dataset of FactSage predictions is provided in Supplementary Materials (Figures S7-S8). At 0% extraction efficiency (no O_2 removed from regolith), the only thermodynamically stable phase is the molten regolith, as expected at BOL. Figure 6(a) presents only the species that are major components of the regolith (Ca, Al) or are involved in electrolysis (Fe, Si, Ti). O is omitted from Figure 6(a) for the sake of clarity but is approximately 60 at% throughout the electrolysis. As the extraction efficiency is increased, cathodic products begin to form in low absolute mass quantities. In Figure 6(b), the normalized composition of cathodic products is presented. There is significant variation in the elemental composition of the cathodic products at low O_2 extraction efficiencies that is attributed to the relatively small mass of cathodic products that initially forms compared with the regolith.

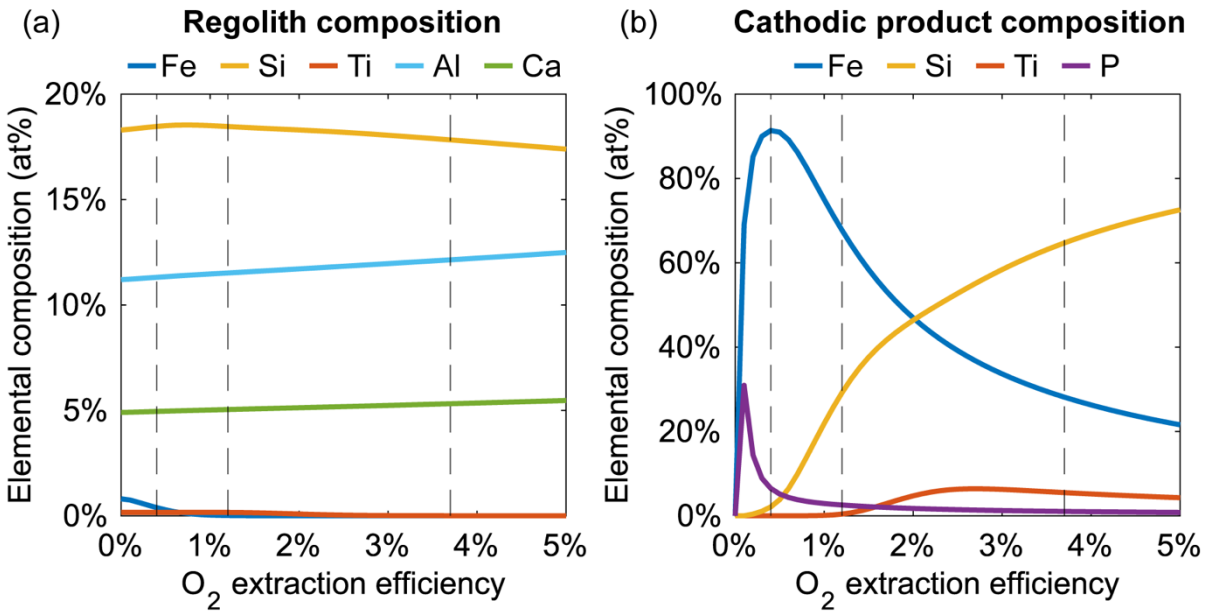

Figure 6: *FactSage predictions of (a) the percent atomic elemental composition of the remaining regolith and (b) the cathodic products composition vs. O_2 extraction efficiency. Dashed vertical lines in (a) and (b) represent the O_2 extraction efficiency achieved in the 1-hour (0.4%), 3-hour (1.2%), and 12-hour (3.7%) electrolysis cells.*

These FactSage predictions generally agree with experimental observations, even though YSZ was not included in the FactSage model. Based on the results from Figure 6(a), it appears that the switchover between predominantly FeO electrolysis to predominantly SiO_2 electrolysis occurs near an O_2 extraction efficiency of 1%. This is consistent with the observation that Si is not present in the cathodic products of the 1-hour electrolysis cell but is present in the cathodic products of the 3-hour electrolysis cell where the electrolysis cell achieved an O_2 extraction efficiency of 1.2%. Similarly, TiO_2 electrolysis is not predicted until an O_2 extraction efficiency of approximately 2%, which agrees with the experimental observation that Ti is not detected in cathodic products until the 12-hour electrolysis cell, which achieved an O_2 extraction efficiency of 3.7%. These results also provide further evidence that the inclusion of YSZ as a solid electrolyte does not significantly impact which oxides are electrolyzed during MRE.

3.5 YSZ interactions

3.5.1 Thermochemically-induced interactions

In previous work, the authors investigated the thermochemical interactions of YSZ in contact with molten regolith simulants and determined that there are two mechanisms at work – specifically, the dissolution of YSZ and the depletion of Y_2O_3 from YSZ [19]. It is expected that both mechanisms are occurring in the electrolysis cells and will eventually lead to YSZ failure in long-term electrolysis experiments. Thus, it is paramount to investigate the rates of dissolution to provide guidance for design lifetimes of YSZ hollow anodes in a MRE environment.

Evidence of YSZ dissolution is observed in the three electrolysis cells. Table 3 shows that Y and Zr are both detected in the solidified LHS-1, indicating that YSZ is dissolving into the molten LHS-1 at operational temperatures. YSZ dissolution by molten silicates is well studied and has been observed in other systems [38]. Previous work by the authors has shown that the

equilibrium solubility of Y and Zr in LHS-1 at 1600°C is approximately 1.4 at% and 1.2 at%, respectively [19]. The measured concentrations of Y and Zr in these electrolysis cells is lower than the solubility limit, which is expected. These experiments were cooled slowly compared to the quenching experiments used to determine the equilibrium solubility of Y and Zr. As a result, the YSZ dissolved into molten LHS-1 is able to nucleate and grow within the molten regolith as the temperature is decreased. Such YSZ particles are observed at the bottom of the 1-hour and 3-hour cells in Figures 3 and 4. The tan-colored opacity observed in the bottom half of the 12-hour electrolysis cell (Figure 5) is also due to YSZ particles that have nucleated from the molten LHS-1 on cooling. EDS maps of YSZ particles from all electrolysis cells are provided in Supplementary Materials (Figures S9-S11).

Furthermore, YSZ wall recession is observed in these electrolysis cells due to dissolution. The recession only occurs where YSZ is in contact with molten LHS-1. Using the portion of YSZ that remains above the molten regolith liquid line as a baseline for the original wall thickness, wall recession is calculated for the YSZ in contact with molten LHS-1. The average wall recession is determined for each electrolysis experiment and summarized in Table 4. The electrolysis durations and the time spent at 1600°C are both provided in Table 4, since it is thermal exposure to molten LHS-1, and not electrolysis itself, that causes YSZ dissolution.

Table 4: *YSZ wall recession due to dissolution by molten LHS-1*

Electrolysis duration	Time at 1600°C	YSZ recession (μm)
1 hr	3 hr	22 ± 10
3 hr	5 hr	54 ± 12
12 hr	14 hr	85 ± 19

Based on Table 4, it appears that the rate of YSZ wall recession is slowing with increasing time in contact with molten LHS-1 at 1600°C. This result suggests that there are additional effects slowing the rate of YSZ dissolution. Kowalski et al. evaluated varying YSZ grain sizes when exposed to molten silicates similar in composition to the molten LHS-1 in this study [39]. They showed that the grain size of YSZ can influence the rate of penetration and dissolution, with larger grains being preferred for minimizing silicate penetration [39]. To better understand YSZ in the current study, EBSD was performed at the YSZ/LHS-1 interface in each cell to generate a grain microstructure map. Additionally, the same EBSD analysis was applied to a piece of YSZ that was not exposed to molten LHS-1 to serve as the BOL reference. The EBSD results are summarized in a grain size histogram, provided in Figure 7.

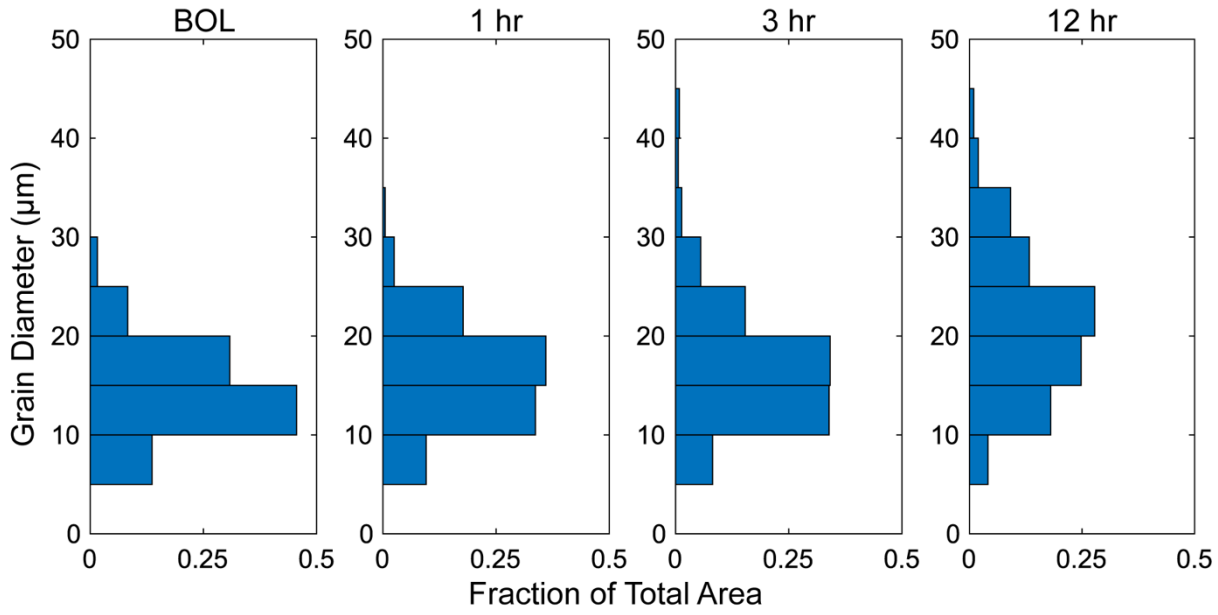

Figure 7: *Area-weighted histogram of YSZ grain diameters (5 μm bins) at beginning-of-life (BOL), 1-hour electrolysis, 3-hour electrolysis, and 12-hour electrolysis.*

From Figure 7, it is clear that grain coarsening is occurring. The molten LHS-1 is penetrating along YSZ grain boundaries and increasing the effective diffusivity of Y_2O_3 and

ZrO_2 along grain boundaries, allowing for coarsening to occur. Increasing durations in contact with molten LHS-1 at 1600°C pushes the average grain diameter to larger values. The slowing of YSZ dissolution is attributed to the grain coarsening behavior discussed here.

It is noted that all three electrolysis cells exhibit YSZ cracking on cooling (seen in Figures 3, 4, and 5). The cracking was observed on the exterior of the cell prior to cross-sectioning. After cross-sectioning, optical and electron microscopy of each cell shows no evidence of regolith penetration along the cracks in the YSZ. These results suggest that the YSZ is cracking on cooling, specifically below the temperature at which LHS-1 solidifies, since cracking while LHS-1 is still liquid would cause the regolith to seep through the YSZ along cracks. This behavior is consistent with what was observed by the authors in previous work using YSZ crucibles to contain LHS-1 [19].

The cause of YSZ cracking is due to Y_2O_3 depletion from the YSZ. Pure ZrO_2 undergoes a monoclinic-to-tetragonal phase transition between 800°C – 1100°C [40]. This phase transition is accompanied by a change in the unit cell volume which gives rise to cracking. Y_2O_3 is a common stabilizer used to suppress this phase transition and allows YSZ to survive thermal cycling. However, exposure to molten regolith causes Y_2O_3 to diffuse out of YSZ and into the molten regolith, forming a YSZ region that is depleted of the Y_2O_3 stabilizer [19]. Due to the low stabilizer content, the YSZ in this region will undergo the tetragonal-to-monoclinic phase transition on cooling. It is this phase transition that causes the YSZ to crack on cooling.

As further evidence, Table 3 shows that average measured concentrations of Y and Zr in the solidified LHS-1 are 0.26 at% and 0.59 at%, resulting in a ratio of Y:Zr of approximately 0.44. In contrast, the ratio of Y:Zr in YSZ at BOL is approximately 0.1, significantly lower than what is observed in the molten regolith. To achieve the 0.44 ratio measured, Y_2O_3 must be

preferentially diffusing out of the YSZ. The EBSD analysis used to determine grain sizes can also provide the crystallographic phase of YSZ and reveals that there is an approximately 100 μm thick layer of YSZ that is monoclinic at the YSZ/LHS-1 interface. EBSD phase maps of YSZ are provided in Supplementary Materials (Figure S12). The presence of monoclinic YSZ at the interface provides further evidence of Y_2O_3 depletion and reveals the cause of YSZ cracking.

3.5.2 Potential-induced interactions

All the electrolysis cells exhibited a decrease in cell resistance after their respective electrolysis periods, with longer durations causing a larger decrease in resistance. A summary of cell resistances is presented in Table 5. There are three contributing factors to the changes in cell resistance – an increase in cathodic surface area, changes in regolith viscosity/conductivity, and the onset of electronic conductivity in YSZ. The cathode surface is already significantly larger than the anode (~10 cm^2 vs ~1 cm^2) at BOL, so an increase in the cathode surface area, resulting from the evolution of liquid cathodic products, is unlikely to cause the magnitude of cell resistance changes observed. The regolith viscosity is inversely related to the regolith electrical conductivity. In the 1-hour electrolysis cell, the removal of FeO/Fe_2O_3 is expected to increase the regolith viscosity, decrease the regolith conductivity, and cause the cell resistance to increase if the regolith viscosity is the dominant factor affecting the cell resistance. However, Table 5 reveals that a resistance decrease is observed in the 1-hour electrolysis cell, indicating that regolith conductivity is not the dominant factor in cell resistance. Thus, the resistance decrease is attributed to the onset of electronic conductivity in the YSZ.

Table 5: *Cell resistances at 1600°C before and after electrolysis*

Electrolysis duration	Initial resistance	Final resistance	% Change
1 hr	1.54 Ω	1.44 Ω	-6.5%
3 hr	1.59 Ω	1.12 Ω	-29.6%
12 hr	1.46 Ω	0.78 Ω	-46.6%

It has been reported in literature that YSZ can have a significant electronic conductivity in low pO_2 environments and/or under an applied DC bias [33–35]. The MRE cell environment exposes YSZ to both conditions, in addition to a higher temperature than typical YSZ applications require. The combination of these factors leads to a high concentration of O^{2-} vacancies forming within the YSZ crystal structure, which can interact with the electrons in the crystal structure to form *F* centers, creating a reduced YSZ structure. These *F* centers give rise to electron states within the band gap of YSZ, allowing high electronic conductivity to exist in a material that is typically an electron insulator [41]. The decrease in cell resistance is a result of this behavior. As a DC bias is applied at 1600°C, more O^{2-} vacancies are formed, allowing for more electron states to open within the band gap of the YSZ, increasing the electronic conductivity of YSZ. This behavior is exacerbated with increasing duration of applied DC potential, thereby resulting in a lower cell resistance (Table 5) with increasing electrolysis duration.

The formation of *F* centers in YSZ not only increases the electronic conductivity of YSZ but also manifests as a darkening in the color of YSZ [41,42]. This effect was also observed in the cells. In Figures 3, 4, and 5, the optical image of the electrolysis cells shows a clear darkening of YSZ from white to gray as the electrolysis duration is increased. The YSZ

darkening behavior is attributed to the formation of *F* centers, resulting from a high concentration of O^{2-} vacancies that form during electrolysis.

Hastak et al. demonstrated that Raman spectroscopy can be used to qualitatively determine the difference in O^{2-} vacancy concentration of YSZ at varying degrees of reduction [43]. Specifically, the A_{1g} Raman mode becomes broader and lower in intensity as the O^{2-} vacancy concentration increases, while the E_g Raman mode is relatively unaffected [43]. Raman spectra of the YSZ in all three electrolysis cells, as well as a BOL sample, are presented in Figure 8. The A_{1g} (260 cm^{-1}) and E_g (640 cm^{-1}) Raman modes are labeled in Figure 8. The Raman spectra are normalized to the intensity of the E_g peak, which is denoted with the horizontal dashed line for each of the spectra. The associated labels summarize the intensity of the A_{1g} peak relative to the E_g peak.

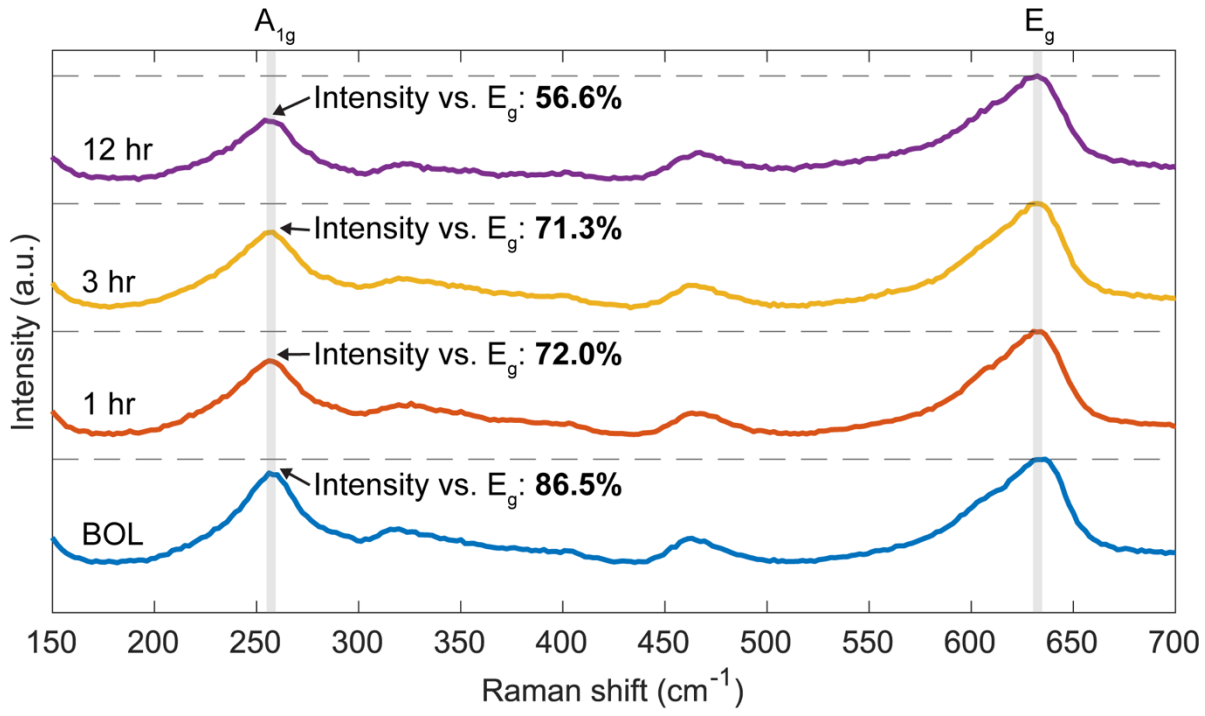

Figure 8: *Raman spectra of YSZ from beginning-of-life (BOL), 1-hour, 3-hour, and 12-hour electrolysis cells.*

The reduction in A_{1g} peak intensity was also observed in the YSZ of the electrolysis cells. The highest intensity YSZ A_{1g} peak occurs in the BOL sample, which has not been reduced or exposed to the MRE conditions. Each electrolysis run shows a decreased A_{1g} intensity compared to the BOL sample, suggesting that more O^{2-} vacancies are present with increasing electrolysis duration. This is consistent with the observed cell resistance behavior (Table 5) and the YSZ color in the electrolysis cells (Figures 3, 4, 5). Based on these results, it is expected that YSZ will become further reduced and electronically conductive with increasing electrolysis duration.

4. Implications for hollow anode design

The results from the *inverted* hollow anode experiments conducted in this study provide insight into how a hollow anode can be incorporated into a MRE reactor. The experimental results presented indicate that MRE can be successfully performed using YSZ/Pt at the anode, without altering the metallic products that form at the cathode. For a hollow anode utilizing YSZ as the solid electrolyte, there are three primary mechanisms affecting electrolysis performance – the onset of electronic conductivity in YSZ, the thermochemical dissolution of YSZ into molten regolith, and the cracking of YSZ induced by Y_2O_3 depletion and thermal cycling. Each mechanism has been previously discussed in the context of the electrolysis experiments performed. In this section, the implications of each mechanism on YSZ hollow anodes in a prototypical MRE reactor are assessed with potential solutions. Additionally, the rate of O_2 generation is compared to the rate of YSZ dissolution to provide an estimate of the anodic mass payback ratio for YSZ hollow anodes.

4.1 YSZ regeneration

The increasing electronic conductivity of YSZ with increasing electrolysis duration is undesirable in a hollow anode application. If YSZ is electronically conductive, O_2 generation is

not isolated to the YSZ/Pt interface and can be produced at the YSZ/regolith interface. Within the hollow anode design, this may cause O_2 to be generated as if the anode were Ir or an ideal inert anode, allowing the produced O_2 to be bubbled through the molten regolith. This would reintroduce bubble separation and reoxidation challenges, resulting in a lower O_2 production efficiency. A method of regenerating YSZ performance is important to enable consistent high O_2 production efficiencies using a hollow anode.

As discussed previously, the electronic conductivity observed in YSZ is due to the formation of reduced YSZ, with a high concentration of O^{2-} vacancies. Thus, the concentration of O^{2-} vacancies must remain low to minimize the electronic conductivity of YSZ. One proposed method of regeneration is to pause MRE after a set amount of time and allow O_2 to dissociate and reabsorb into the YSZ crystal structure (reoxidation), filling the excess O^{2-} vacancies. The reversible uptake of O_2 into YSZ and subsequent metal-to-insulator transition is well studied [44]. However, further work is necessary to determine the correct conditions (pO_2 and duration) to regenerate the performance of YSZ in a hollow anode application. Guo et al. investigated the thermochemical darkening of YSZ for oxygen sensor applications in low pO_2 environments and provided a similar suggestion that YSZ should be periodically reoxidized to prolong the performance of YSZ [42]. The same type of thermochemical reoxidation is proposed here to reduce the electronic conductivity of YSZ, increasing the O_2 production efficiency of the hollow anode. Based on Figure 2, it appears that regeneration should be performed approximately every 6 hours if the same current density (0.5 A/cm^2) is used.

4.2 Design life

YSZ undergoes dissolution in contact with molten regolith. For highlands regolith, this process appears to be relatively slow when compared to the timescale of increasing YSZ

electronic conductivity. From Table 4, an average of 85 μm of wall recession was observed for 12 hours of electrolysis, providing a wall recession rate of approximately 7 μm/hr. Linearly extrapolating these values suggests that a week of operation would result in approximately 1.2 mm of recession, roughly 40% of the original YSZ wall thickness. Based on these values, it appears that a YSZ hollow anode would need to be changed out every one to two weeks if used continuously in contact with highlands regolith. However, these results do not account for the decrease in the rate of YSZ wall recession that stems from grain coarsening at the interface. Thus, the conservative design life of one to two weeks is likely a lower bound on the usable life of YSZ in contact with molten highlands regolith. It is possible that grain coarsening can significantly decrease the rate of YSZ dissolution and extend the design life of YSZ hollow anodes, but further experiments are needed to quantify the expected design life of YSZ hollow anodes.

4.3 Thermal cycling behavior

The Y_2O_3 depletion caused by interactions between YSZ and molten regolith will cause YSZ to crack on cooling. Since no regolith penetration is detected along YSZ cracks in the inverted hollow anode, the cracks are assumed to form below the solidification temperature of LHS-1. This behavior indicates that YSZ hollow anodes are expected to survive through only a single thermal cycle. However, given the relatively long usable life of YSZ, the expectation is that MRE reactors incorporating a hollow anode would not be thermally cycled until the design life of the YSZ is reached (one to two weeks). Since the cracking would occur after the usable life of a YSZ hollow anode is reached, it would be replaced regardless. Large-scale O_2 production rates (>10 MT/year) are necessary to meet NASA's production goal for a technology demonstration [45], which will likely require an MRE reactor to operate continuously and with a

high duty cycle. The continuous operation of a MRE reactor will decrease the number of thermal cycles, ideally extending high temperature operation to the full design life of a YSZ hollow anode.

4.4 Anode mass payback ratio

Given that YSZ hollow anodes exhibit dissolution in molten regolith, it is paramount to assess the tradeoff between oxygen production and anode material loss over time. For this analysis, a YSZ anode with dimensions of 1 cm × 1 cm and a wall thickness of 0.3 cm is considered, consistent with the geometry of the cells utilized in this study. Based on the manufacturer-reported density of 5.92 g/cm³, this anode has a mass of approximately 1.78 g. Due to observed thermal cycling-induced cracking, it is conservatively assumed that the full mass of the anode is lost upon reaching the end of its design life. From the 12-hour electrolysis tests reported in Tables 2 and 4, the average anode wall recession rate is 7 μm/hr, while the corresponding average O_2 production rate is 0.062 g/hr. Assuming anode replacement is required upon dissolution of half the wall thickness, the projected operational lifetime is approximately 214 hours (~8.9 days). Over this duration, the anode is expected to produce approximately 13.4 g of O_2. This yields an anode mass payback ratio of approximately 7.5, defined as the mass of O_2 produced per unit mass of YSZ consumed.

It is important to note that this estimate assumes a constant rate of O_2 production and YSZ recession, both of which require further testing to validate. Additionally, this analysis excludes the mass of the MRE system and the cathode but also does not account for the mass of cathodic products generated, which has value for in-situ construction/manufacturing. Overall, these results suggest that each unit mass of YSZ delivered to the lunar surface could enable the production of up to 7.5 times its own mass in O_2 under the assumed conditions.

5. Conclusions

This study presents the hollow anode as an alternative anode design to the state-of-the-art Ir anodes currently used in MRE reactors. The hollow anode allows for the facile collection of O_2 by utilizing a YSZ solid electrolyte in combination with a Pt current collector, allowing produced O_2 to be removed without contacting the molten regolith. This design addresses both the bubble formation and reoxidation challenges associated with MRE. Additionally, the hollow anode can be a more cost-effective solution compared with bare Ir anodes.

Experimental results from an inverted hollow anode reactor demonstrate that MRE can be successfully performed through a YSZ solid electrolyte for up to 12 hours. Residual gas analysis indicates that O_2 is produced when a constant current is applied to the cell, confirming that anodic O_2 production is not affected by the YSZ solid electrolyte. Subsequent SEM/EDS analysis of the cross-sectioned cells reveal the compositions of both the cathodic products and solidified regolith simulant. The primary cathodic products are Fe and Si, which is consistent with previous MRE models. Furthermore, the FeO and SiO_2 content of the solidified regolith simulant decreases with increasing electrolysis duration, indicating that FeO and SiO_2 electrolysis is achieved in the inverted hollow anode reactor. To the authors' knowledge, this is the first reported experimental confirmation of SiO_2 electrolysis in a MRE reactor. This is significant since SiO_2 is the most abundant oxide species in lunar regolith. Demonstrating O_2 production from SiO_2 provides confirmation that high O_2 electrolysis efficiencies (>25%) are possible through MRE utilizing a hollow anode.

Post-electrolysis analysis of the YSZ reveals that there are three primary mechanisms affecting electrolysis performance - the onset of electronic conductivity in YSZ, the thermochemical dissolution of YSZ into molten regolith, and the cracking of YSZ, induced by

Y_2O_3 depletion and thermal cycling. The rates associated with each mechanism are estimated from the inverted hollow anode cells. From these rates, preliminary design guidelines for YSZ hollow anodes in a prototypical MRE reactor are identified. Given the extreme operating environment of MRE, the observed interactions between YSZ and LHS-1 are expected. However, the overall dissolution rate of YSZ indicates that electrolysis durations longer than the 12 hours achieved in this study are possible, potentially allowing for a YSZ hollow anode to operate for up to two weeks. By comparing the measured rates of YSZ dissolution and O_2 production, it was determined that YSZ hollow anodes can produce up 7.5 times their mass in O_2.

The inverted hollow anode experiments provide a promising proof-of-principle, demonstrating that the hollow anode design can potentially address some of the key challenges associated with MRE. These results pave the way for the next phase of development that focuses on higher fidelity testing to fully evaluate YSZ hollow anodes in a relevant environment that includes lunar surface ambient temperatures and lunar vacuum. Future research presents opportunities to integrate YSZ hollow anodes into existing MRE reactors, enabling direct comparisons with bare Ir anodes. While the initial inverted hollow anode experiments presented here are encouraging, further work will help determine the life-cycle cost and scalability of operating a full-scale MRE reactor utilizing a hollow anode.

Acknowledgements

This work was supported by a NASA Space Technology Graduate Research Opportunity (Grant #: 80NSSC22K1184) for K. Yu, K. T. Faber, and L. Reidy. W. West and J. Dominguez were consulted as subject matter experts as part of the NASA Space Technology Graduate Research Opportunity. J. Stokes and B. Harder were supported by NASA Aeronautics Research Mission Directorate's Transformational Tools and Technologies Project. The research was carried out in part at the Jet Propulsion Laboratory, California Institute of Technology, under a contract with the National Aeronautics and Space Administration (80NM0018D0004). The authors gratefully acknowledge Dr. Chi Ma of the Caltech Geology and Planetary Sciences Analytical Facility for his assistance with EBSD and Professor George Rossman for assistance with the confocal Raman microscope. The authors would like to thank Dr. Thierry Caillat at the Jet Propulsion Laboratory for providing the residual gas analyzer used to track O_2 production and Dr. Nicholas Heinz at the Jet Propulsion Laboratory for the use of their optical microscopy facilities. The authors would also like to thank Dr. Donald Dornbusch and Dr. Will Huddleston at NASA Glenn Research Center for helpful discussions and support in analyzing the molten regolith electrolysis data. The authors would also like to thank Professor Jean-Philippe Harvey for his assistance with establishing the FactSage thermochemical model used in this study.

References

[1] A. Cassel, Forward to the Moon: NASA's Strategic Plan for Human Exploration, (2019). https://ntrs.nasa.gov/citations/20190032000.

[2] V. Badescu, ed., Moon: Prospective Energy and Material Resources, Springer Berlin Heidelberg, Berlin, Heidelberg, 2012. https://doi.org/10.1007/978-3-642-27969-0.

[3] NASA, SLS (Space Launch System) Core Stage, (2024). https://www.nasa.gov/reference/sls-space-launch-system-core-stage/ (accessed December 23, 2024).

[4] V. Maiwald, M. Bauerfeind, S. Fälker, B. Westphal, C. Bach, About feasibility of SpaceX's human exploration Mars mission scenario with Starship, Sci Rep 14 (2024) 11804. https://doi.org/10.1038/s41598-024-54012-0.

[5] P.T. Metzger, Economics of in-space industry and competitiveness of lunar-derived rocket propellant, Acta Astronautica 207 (2023) 425–444. https://doi.org/10.1016/j.actaastro.2023.03.014.

[6] L. Schlüter, A. Cowley, Review of techniques for In-Situ oxygen extraction on the moon, Planetary and Space Science 181 (2020) 104753. https://doi.org/10.1016/j.pss.2019.104753.

[7] P. Zhang, W. Dai, R. Niu, G. Zhang, G. Liu, X. Liu, Z. Bo, Z. Wang, H. Zheng, C. Liu, H. Yang, Y. Bai, Y. Zhang, D. Yan, K. Zhou, M. Gao, Overview of the Lunar In Situ Resource Utilization Techniques for Future Lunar Missions, Space Sci Technol 3 (2023) 0037. https://doi.org/10.34133/space.0037.

[8] S.S. Schreiner, L. Sibille, J.A. Dominguez, J.A. Hoffman, A parametric sizing model for Molten Regolith Electrolysis reactors to produce oxygen on the Moon, Advances in Space Research 57 (2016) 1585–1603. https://doi.org/10.1016/j.asr.2016.01.006.

[9] F.J. Guerrero-Gonzalez, P. Zabel, System analysis of an ISRU production plant: Extraction of metals and oxygen from lunar regolith, Acta Astronautica 203 (2023) 187–201. https://doi.org/10.1016/j.actaastro.2022.11.050.

[10] E. Standish, D. Stefanescu, P. Curreri, Ceramics for Molten Materials Containment, Transfer and Handling on the Lunar Surface, in: 47th AIAA Aerospace Sciences Meeting Including The New Horizons Forum and Aerospace Exposition, American Institute of Aeronautics and Astronautics, Orlando, Florida, 2009. https://doi.org/10.2514/6.2009-1657.

[11] A. Allanore, Features and Challenges of Molten Oxide Electrolytes for Metal Extraction, J. Electrochem. Soc. 162 (2014) E13. https://doi.org/10.1149/2.0451501jes.

[12] H. Kim, J.D. Paramore, A. Allanore, D.R. Sadoway, Stability of Iridium Anode in Molten Oxide Electrolysis for Ironmaking: Influence of Slag Basicity, ECS Trans. 33 (2010) 219. https://doi.org/10.1149/1.3484779.

[13] H. Kim, J. Paramore, A. Allanore, D.R. Sadoway, Electrolysis of Molten Iron Oxide with an Iridium Anode: The Role of Electrolyte Basicity, J Electrochem Soc 158 (2011) E101. https://doi.org/10.1149/1.3623446.

[14] D. Wang, A.J. Gmitter, D.R. Sadoway, Production of Oxygen Gas and Liquid Metal by Electrochemical Decomposition of Molten Iron Oxide, J. Electrochem. Soc. 158 (2011) E51. https://doi.org/10.1149/1.3560477.

[15] M.S. Humbert, G.A. Brooks, A.R. Duffy, C. Hargrave, M.A. Rhamdhani, Thermophysical property evolution during molten regolith electrolysis, Planet Space Sci 219 (2022) 105527. https://doi.org/10.1016/j.pss.2022.105527.

[16] B.A. Lomax, G.H. Just, P.J. McHugh, P.K. Broadley, G.C. Hutchings, P.A. Burke, M.J. Roy, K.L. Smith, M.D. Symes, Predicting the efficiency of oxygen-evolving electrolysis on the Moon and Mars, Nat Commun 13 (2022) 583. https://doi.org/10.1038/s41467-022-28147-5.
[17] P.A. Burke, M.E. Nord, C.A. Hibbitts, J.R. Berdis, Modeling electrolysis in reduced gravity: producing oxygen from in-situ resources at the moon and beyond, Front. Space Technol. 5 (2024). https://doi.org/10.3389/frspt.2024.1304579.
[18] K. Grossman, E. Petersen, E. Bell, J. Toro-Medina, L. Sibille, H. Williams, T. Newbold, K. Zacny, I. Bates, GaLORE (Gaseous Lunar Oxygen from Regolith Electrolysis): Successful Demonstration of a Cold-Walled Molten Regolith Electrolysis Reactor Design in a vacuum environment, (2023). https://isruinfo.com/public/docs/srr23/10-4%20Grossman-GALORE%20Demonstration%20of%20a%20Cold-Walled%20Molten%20Regolith%20Electrolysis%20Reactor%20Design%20in%20a%20Vacuum%20Environment.zip (accessed December 23, 2024).
[19] K. Yu, J. Stokes, B. Harder, L. Reidy, K.T. Faber, Thermochemical interactions between yttria-stabilized zirconia and molten lunar regolith simulants, Journal of the American Ceramic Society 107 (2024) 7119–7130. https://doi.org/10.1111/jace.19821.
[20] C.A. Krier, R.I. Jaffee, Oxidation of the platinum-group metals, Journal of the Less Common Metals 5 (1963) 411–431. https://doi.org/10.1016/0022-5088(63)90055-9.
[21] J. Guo, T. Villalon, U. Pal, S. Basu, Effect of optical basicity on the stability of yttria-stabilized zirconia in contact with molten oxy-fluoride flux, J Am Ceram Soc 101 (2018) 3605–3616. https://doi.org/10.1111/jace.15496.
[22] Y. Gao, C. Duan, Y. Yang, D. Ruan, C. Yang, C. Hong, Effect of Applied Voltage on Electroreduction with Controlled Oxygen Flow of Molten Slag Containing FeO at 1723 K, ISIJ International 55 (2015) 2273–2282. https://doi.org/10.2355/isijinternational.ISIJINT-2014-826.
[23] Y. Gao, C. Yang, C. Zhang, Q. Qin, G.Z. Chen, Magnesia-stabilised zirconia solid electrolyte assisted electrochemical investigation of iron ions in a SiO_2–CaO–MgO–Al_2O_3 molten slag at 1723 K, Phys. Chem. Chem. Phys. 19 (2017) 15876–15890. https://doi.org/10.1039/C7CP01945A.
[24] NASA, Why Artemis will focus on the Lunar South Pole region, 2022. https://www.lpi.usra.edu/lunar/artemis/resources/WhitePaper_2023_WhyLunarSouthPolarRegion.pdf.
[25] M.P. Lucas, C.R. Neal, J.M. Long-Fox, D. Britt, Simulating lunar highlands regolith profiles on Earth to inform infrastructure development and ISRU activities on the Moon, Acta Astronautica 224 (2024) 161–171. https://doi.org/10.1016/j.actaastro.2024.08.019.
[26] Space Resource Technologies, LHS-1 Lunar Highlands Simulant Fact Sheet (002-01-001-0621), (2021). https://cdn.shopify.com/s/files/1/0398/9268/0862/files/lhs-1-spec-sheet-Dec2022.pptx.pdf?v=1688051876.
[27] J.J. Papike, S.B. Simon, J.C. Laul, The lunar regolith: Chemistry, mineralogy, and petrology, Reviews of Geophysics 20 (1982) 761–826. https://doi.org/10.1029/RG020i004p00761.
[28] H.M. Sargeant, F.A.J. Abernethy, S.J. Barber, I.P. Wright, M. Anand, S. Sheridan, A. Morse, Hydrogen reduction of ilmenite: Towards an in situ resource utilization demonstration on the surface of the Moon, Planetary and Space Science 180 (2020) 104751. https://doi.org/10.1016/j.pss.2019.104751.

[29] C.A. Schneider, W.S. Rasband, K.W. Eliceiri, NIH Image to ImageJ: 25 years of image analysis, Nat Methods 9 (2012) 671–675. https://doi.org/10.1038/nmeth.2089.
[30] F. Bachmann, R. Hielscher, H. Schaeben, Grain detection from 2d and 3d EBSD data—Specification of the MTEX algorithm, Ultramicroscopy 111 (2011) 1720–1733. https://doi.org/10.1016/j.ultramic.2011.08.002.
[31] C.W. Bale, E. Bélisle, P. Chartrand, S.A. Decterov, G. Eriksson, A.E. Gheribi, K. Hack, I.-H. Jung, Y.-B. Kang, J. Melançon, A.D. Pelton, S. Petersen, C. Robelin, J. Sangster, P. Spencer, M.-A. Van Ende, FactSage thermochemical software and databases, 2010–2016, Calphad 54 (2016) 35–53. https://doi.org/10.1016/j.calphad.2016.05.002.
[32] R.I. Webster, E.J. Opila, Viscosity of CaO-MgO-Al2O3-SiO2 (CMAS) melts: Experimental measurements and comparison to model calculations, J Non-Cryst Solids 584 (2022) 121508. https://doi.org/10.1016/j.jnoncrysol.2022.121508.
[33] N. Masó, A.R. West, Electronic Conductivity in Yttria-Stabilized Zirconia under a Small *dc* Bias, Chem. Mater. 27 (2015) 1552–1558. https://doi.org/10.1021/cm503957x.
[34] R. Kirchheim, On the mixed ionic and electronic conductivity in polarized yttria stabilized zirconia, Solid State Ionics 320 (2018) 239–258. https://doi.org/10.1016/j.ssi.2018.03.014.
[35] M. Jovaní, H. Beltrán-Mir, E. Cordoncillo, A.R. West, Field-induced p-n transition in yttria-stabilized zirconia, Sci Rep 9 (2019) 18538. https://doi.org/10.1038/s41598-019-54588-y.
[36] A.H. Sirk, D.R. Sadoway, L. Sibille, Direct Electrolysis of Molten Lunar Regolith for the Production of Oxygen and Metals on the Moon, ECS Transactions 28 (2010) 367–373. https://doi.org/10.1149/1.3367929.
[37] J. Houserová, J. Vřešťál, M. Šob, Phase diagram calculations in the Co–Mo and Fe–Mo systems using first-principles results for the sigma phase, Calphad 29 (2005) 133–139. https://doi.org/10.1016/j.calphad.2005.06.002.
[38] C.S. Holgate, G.G.E. Seward, A.R. Ericks, D.L. Poerschke, C.G. Levi, Dissolution and diffusion kinetics of yttria-stabilized zirconia into molten silicates, J Eur Ceram Soc 41 (2021) 1984–1994. https://doi.org/10.1016/j.jeurceramsoc.2020.10.056.
[39] B. Kowalski, J. Stokes, P.E. Albert, P.E. Lauer, D.E. Wolfe, Effect of test parameters in the exposure of Ca–Mg–Al–silicate on yttria stabilized zirconia, J Am Ceram Soc 106 (2023) 3911–3921. https://doi.org/10.1111/jace.19025.
[40] G.M. Wolten, Diffusionless Phase Transformations in Zirconia and Hafnia, Journal of the American Ceramic Society 46 (1963) 418–422. https://doi.org/10.1111/j.1151-2916.1963.tb11768.x.
[41] V.R. PaiVerneker, A.N. Petelin, F.J. Crowne, D.C. Nagle, Color-center-induced band-gap shift in yttria-stabilized zirconia, Phys. Rev. B 40 (1989) 8555–8557. https://doi.org/10.1103/PhysRevB.40.8555.
[42] Xin Guo, Yao-Qing Sun, Kun Cui, Darkening of zirconia: a problem arising from oxygen sensors in practice, Sensors and Actuators B: Chemical 31 (1996) 139–145. https://doi.org/10.1016/0925-4005(96)80058-X.
[43] V. Hastak, E.J. Gildersleeve, S. Batna, A.S. Gandhi, S. Sampath, On the oxygen vacancy annealing in air plasma sprayed yttria-stabilized zirconia thermal barrier coatings, J Am Ceram Soc. 107 (2024) 920–932. https://doi.org/10.1111/jace.19477.
[44] A. Alvarez, Y. Dong, I.-W. Chen, DC electrical degradation of YSZ: Voltage-controlled electrical metallization of a fast ion conducting insulator, Journal of the American Ceramic Society 103 (2020) 3178–3193. https://doi.org/10.1111/jace.17004.

[45] NASA, Lunar Infrastructure Foundational Technologies-1: Request for Information, (2023). https://nspires.nasaprs.com/external/viewrepositorydocument/cmdocumentid=967421/solicitationId=%7B23D0FE0E-099D-77A8-3E06-2C516D900762%7D/viewSolicitationDocument=1/LIFT-1%20RFI%20STMD%20Amednment%201.pdf (accessed December 23, 2024).